Transport in Porous Media (2018) 124:1061–1079
https://doi.org/10.1007/s11242-018-1110-6

Numerical Simulation of the Fluid–Solid Coupling Process During the Failure of a Fractured Coal–Rock Mass Based on the Regional Geostress

P. F. Shan[1] · **X. P. Lai**[1]

Received: 31 January 2018 / Accepted: 22 June 2018 / Published online: 29 June 2018

Abstract
This paper presents a numerical approach to the simulation of fluid–solid coupling during the failure of a fractured coal–rock mass taking into consideration the regional geostress characteristics. We use the back calculation method to calculate the regional geostress of the study area, and we verify the accuracy of the back calculation method based on the in situ monitoring data. The values of the vertical stress and the minimum principal horizontal stress used in the numerical simulation are 7.057 and 8.085 MPa, respectively. In addition, the maximum principal horizontal stress has a local undulation that is affected by excavation disturbance. With a newly developed mechanical experimental system for digital radiography scanning, the temporal–spatial evolution of the fracture field is also revealed. The main fractures continue to propagate with increased external loading, and the spatial form of the fracture fields is a conjugate pattern and an X-shaped pattern. Based on the COMSOL Multiphysics program, the results indicate that the primary reason for crack propagation and connection is increased external loading, which leads to macroscopic fracturing of the coal–rock mass and incremental changes in the average porosity and permeability. The flow within the maximum velocity region represents the distribution characteristics of the induced cracks. The peak flow velocity is located at the main fracture, and its direction is parallel to that of the water injection pressure. Smaller fractures have a larger hydraulic gradient and larger flow velocities than larger fractures. The water outlet velocity characteristics indicate that the maximum flow velocity in the water outlet is located on the two sides of the model and increases with increasing external loading. All the fluid–solid coupling mechanisms would provide a reliable theoretical basis for optimization of mined-void roof weakening in mining the steeply inclined coal seam.

Keywords Steeply inclined coal seam · Simulation model · Rock mass · Fluid–solid coupling · Regional geostress

✉ P. F. Shan
shanpengfei571571@126.com

[1] School of Energy Engineering, Xi'an University of Science and Technology, Xi'an 710054, China

1 Introduction

Many protogenetic geological structures are randomly distributed throughout natural rock masses. These structures include flaws, pores, fissures, and fractures. The regional geostress causes these structures to evolve into stress concentration-release zones, which reduce the stability of the rock mass significantly. In particular, the partial stress alters the intrinsic permeability of the fractured rock mass. In turn, the hydrological alternation alters the regional geostress field. For this reason, the mechanical–hydrological coupling effect is a key factor when investigating fractured rock mass mechanics (Xie et al. 2015).

There are a substantial number of coal seams in the Urumchi coal field, which is located in the northwestern meizoseismal region of China (Dzungaria Basin). The thicknesses of these seams are greater than 30.0 m, and the angles exceed 45°, i.e., extremely steep and thick coal seams (ESTCS) (Lai et al. 2016). Approximately 3.6 billion tons of this coal falls into the ESTCS category (Zhang and Lai 2008). The mechanized sub-horizontal section top-coal caving (SSTCC) method, a specific type of top-coal caving (Xie and Zhao 2009), is a powerful method for extracting the ESTCC in the Urumchi coal field. In such a complicated geological and mining setting, failure of the overlying strata after coal caving may be induced by the hybrid physical–mechanical coupling effect of the regional stress, excavation disturbance stress, and seismic forces (Alehossein and Poulsen 2010; Lai et al. 2014). In addition, a generous seasonal water source (snow melt) remains in the overlying strata and becomes a confined aquifer above the caving face (Zhang et al. 2017). After top-coal caving, the surrounding rocks experience structural distortion and their strength decreases, which can be revealed by the effects of fracture-hydrological coupling. It is possible for a marco-fracturing network to provide a path for the confined aquifer to flow toward the current caving face. Sometimes, a confined aquifer with abundant clays, sand, and stone results in dynamic hazard events, such as water burst and sand inrush onto the stope. In addition, the mechanical properties of the overlying strata are significantly degraded when the rock mass is immersed in water for a long period of time, and the mechanical property degradation makes the overlying strata extremely susceptible to large-scale ruptures and induces rock burst near the caving face. Even worse, underground debris flows may occur frequently. All of these dynamic events are potentially dangerous to the staff and facilities (Simsir and Ozfirat 2008; Lauriello and Fritsch 1974; Kelly et al. 2001).

In the Urumchi coal field, strong crushing stress is the predominant stress. According to previous studies, minute changes in the fracture width can cause tremendous changes in the seepage flux (Zhu et al. 2009; Zhang and Zhang 1997; Allen et al. 2005; Scesi and Gattinoni 2007; Zhao et al. 2008; Jafari et al. 2004). The fracture width is subject to the stress, and the seepage flux is closely related to the regional geostress. In addition, the hydraulic seepage pressure immediately impacts the effective stress of the fracture plane. Thus, the mechanical-fracture coupling effect also increases the deterioration of the rock mass. In general, when studying the seepage mechanism of fractures, the regional geostress should be considered in the determination of the multi-field coupling effect.

In the field of mechanics, water–rock interaction is called fluid–solid coupling, and many scholars have highlighted analytical models and numerical simulations for use with multi-field coupling (Oda 1986; Wu 1995; Wang et al. 1996). In the field of earth science, however, recent research on water–rock interaction emphasizes the fluid–solid coupling model of rock mass hydraulics, the rock fracturing process, and its failure mechanism. In addition, the physical and chemical effects of water on the mechanical properties have received more

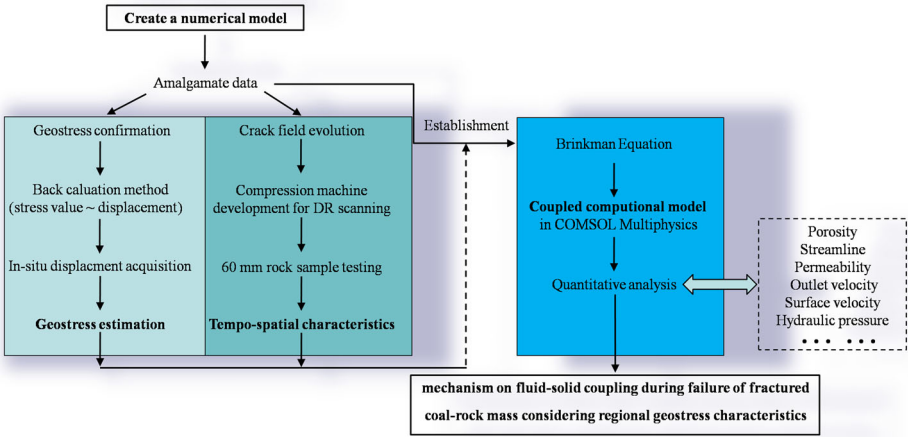

Fig. 1 Analytical methodology for assessing fluid–solid coupling mechanism during failure of a fractured coal–rock mass taking into account the regional geostress characteristics

attention (Feng and Masahiro 2000; Huang et al. 2008; Tang et al. 2002, 2010), but correlation studies are seldom concerned with the regional geostress.

The northwestern part of China is the main region of energy resource production; it is a tectonically active region and is ecologically fragile with an arid to semiarid climate. Therefore, water conservation during coal mining in the northwestern part of China is imperative. In 2015, the Ministry of science and technology of the People's Republic of China implemented National key basic research and development plan No. 2015CB25162, China (973 Plan), with the goal of conserving water resources during coal mining in the northwestern part of China. One of the project's goals was to develop a valid fluid–solid coupling mechanism for the failure of a fractured coal–rock mass taking into consideration the regional geostress. The mechanism was also used as the theoretical basis for the entire project.

Based on the above viewpoints, in this paper, we develop a new analytical method. Figure 1 illustrates the analytical method including the development of a numerical model, which incorporates an innovative experimental technique that accounts for the fluid–solid coupling that occurs during failure of a fractured coal–rock mass and takes into account the regional geostress. We also describe the detailed development of this simulation model, which involves the amalgamation of the back calculation of the regional geostress, assessment of the temporal–spatial characteristics of the fracture field, and a coupled computation model that uses the above-mentioned conditions. In order to ensure the rationality and consistency of the method, all of the models were cubes with side lengths of 60 mm, which is in accordance with the relative rock test standard of the International Society of Rock Mechanics and Engineering (ISRM).

2 Numerical Simulation

2.1 Back Calculation of the Regional Geostress

In this paper, the site for which the back calculation was performed was located at the southern lane of the No. 45 fully mechanized top-coal caving face on the + 500 level of the Wudong coal

mine, in the Urumchi coal field. In particular, all mechanical experiment samples involved in follow-up assignments were collected in this site.

The southern coal lane is a rectangle, with a width of 4.4 m and a height of 3.4 m. Based on previous research, lane excavation of the steeply inclined coal seams produced an equivalent nodal force acting on the excavation boundary of the coal–rock masses. Here, a quantifiable relationship between the equivalent nodal force and the regional geostress is described by a volume integral as follows:

$$\bar{\boldsymbol{P}} = \int_{\mathrm{V}} \bar{\boldsymbol{B}}^{\mathrm{T}} \boldsymbol{\sigma} \, \mathrm{d}\boldsymbol{V}. \tag{1}$$

where $\bar{\boldsymbol{P}}$ is the equivalent nodal force on the excavation boundary of the coal–rock masses; σ is the regional geostress; and $\bar{\boldsymbol{B}}$ is the strain matrix of the boundary after excavation and depends on the geometry of the surrounding excavated rock. In the back calculation, the southern lane was simplified as a 2D plane problem, so $\boldsymbol{\sigma} = \{\sigma_x, \sigma_y, \tau_{xy}\}^{\mathrm{T}}$. Specifically, σ_z, which is parallel to the lane's strike, is non-accountable in the calculation. Therefore, Eq. (1) becomes Eq. (2).

$$\bar{\boldsymbol{P}} = \sigma_x \bar{\boldsymbol{B}}^1 + \sigma_y \bar{\boldsymbol{B}}^2 + \tau_{xy} \bar{\boldsymbol{B}}^3. \tag{2}$$

where $\bar{\boldsymbol{B}}^i$ $(i = 1, 2, 3)$ is the component function of $\boldsymbol{B}$. In addition, we determined the relation between $\bar{\boldsymbol{P}}$ and the nodal displacement $(\boldsymbol{u})$ to be

$$\bar{\boldsymbol{P}} = \boldsymbol{K}\boldsymbol{u}. \tag{3}$$

where $\boldsymbol{K}$ is the stiffness matrix of the entire excavated zone. On the excavated boundary, $\boldsymbol{P}$ and $\bar{\boldsymbol{P}}$ are the same. In addition, the forces at the internal nodes are zero. By combining Eqs. (2) and (3), we obtain Eq. (4).

$$\boldsymbol{K}\boldsymbol{u} = \sigma_x \boldsymbol{B}^1 + \sigma_y \boldsymbol{B}^2 + \tau_{xy} \boldsymbol{B}^3. \tag{4}$$

here we assume that the measurement points of lane displacement are all enclosed by finite element grid nodes. Thus, $\boldsymbol{u}$ can be divided into two parts: the displacement values of the measured points $(\boldsymbol{u}^1)$ and the displacement values of the unmeasured points $(\boldsymbol{u}^2)$, as is shown by Eq. (5).

$$\boldsymbol{u} = \left\{\boldsymbol{u}^1, \boldsymbol{u}^2\right\}^{\mathrm{T}}. \tag{5}$$

By combining Eqs. (4) and (5), we eliminate $\boldsymbol{u}^2$ and obtain Eq. (6).

$$\begin{cases} \boldsymbol{u}^1 = \boldsymbol{A}\boldsymbol{\sigma}^0 \\ \boldsymbol{A} = \left[\boldsymbol{K}_2^{*-1}\boldsymbol{B}_x,\ \boldsymbol{K}_2^{*-1}\boldsymbol{B}_y,\ \boldsymbol{K}_2^{*-1}\boldsymbol{B}_{xy}\right] \\ \boldsymbol{\sigma}^0 = \left\{\sigma_x/E,\ \sigma_y/E,\ \tau_{xy}/E\right\}^{\mathrm{T}} \end{cases} \tag{6}$$

There are three variables in Eq. (6): σ_x/E, σ_y/E and τ_{xy}/E. E is elastic modulus for a constant coal–rock mass, which was confirmed by a mechanical experiment. In situ measurements were used for both the amount of coal–rock mass movement and the sectional convergence. Three sets of surrounding rock movement censors were arranged at 150, 200, and 250 m along the southern lane (Fig. 2). Each set consisted of six GYW-300 censors. We input the acquired data into Eq. (6) to determine the regional geostress near the excavation boundary as is shown in Table 1. The back calculation results for the vertical geostress, the minimum principal horizontal stress, and the shearing stress were 7.057, 8.085, and 0.057 MPa, respectively.

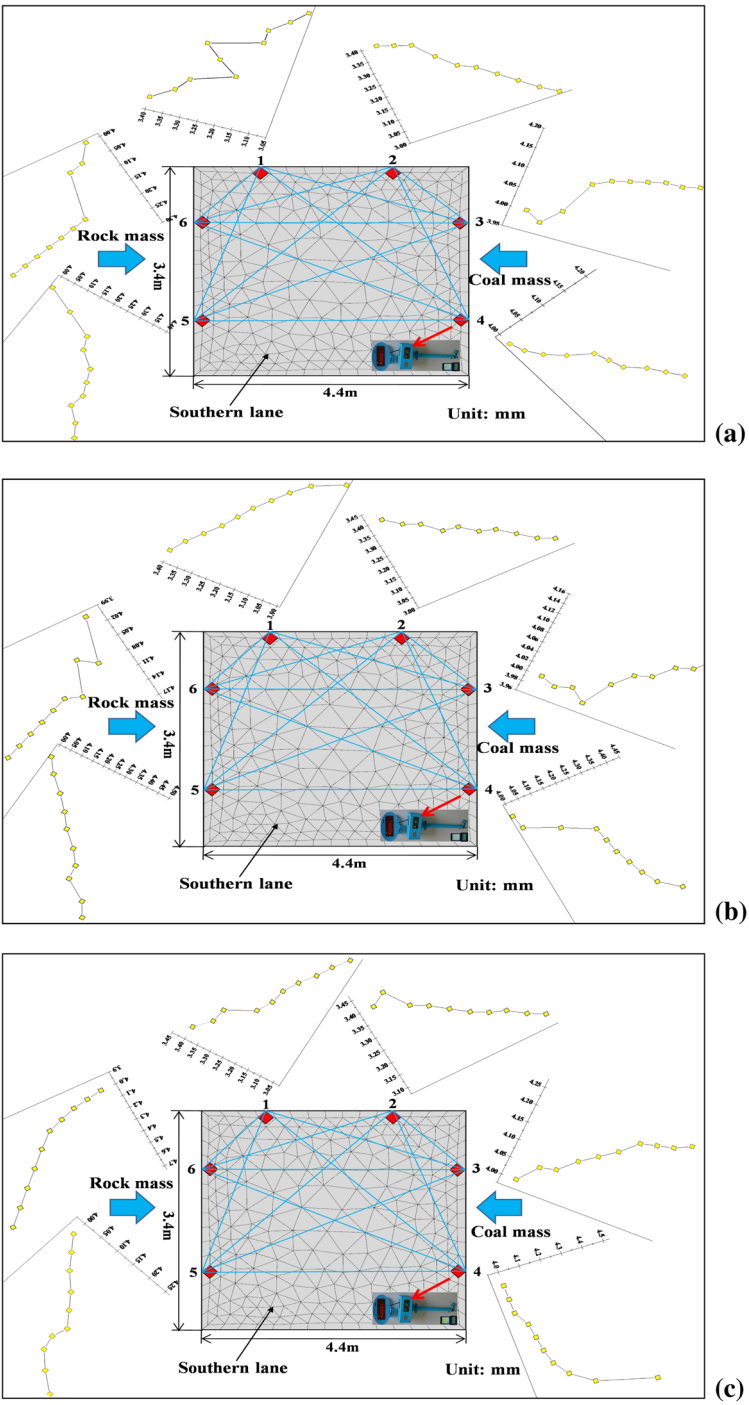

Fig. 2 Statistical results of data from the movement censors in the surrounding rock **a** 150 m; **b** 200 m; and **c** 250 m

Table 1 Relevant results of the back-calculated analysis of the regional geostress

Variable (MPa)	σ_x^0	σ_y^0	τ_{xy}^0	σ_{xi}	σ_{yi}	τ_{xyi}
Position (m)						
150	0.01029	0.01191	0.00009	7.056	8.170	0.059
200	0.01029	0.01148	0.00008	7.059	7.875	0.058
250	0.01028	0.01197	0.00008	7.055	8.211	0.055

The KJ743 coal mine geostress monitoring system was used to collect real-time stress data, which we used to check the accuracy of the back calculation results. The censors in the system have been setup at 180, 220, 250, 290, 330, 360, 400, and 430 m (Fig. 3a). Each censor consisted of a deep point and a shallow point censor with burial depths of 10.0 and 5.0 m, respectively. Figure 3 shows the real-time monitoring results from the geostress monitoring system. Figure 3b is a plot of the stress data from November 11, 2014 to February 2, 2015. The vertical geostress was remained fairly constant with small fluctuation within a narrow range due to disturbance from the excavation occurring in this area. The value of the vertical geostress varied from 6.8 to 7.0 MPa, which is slightly smaller than the result of the back calculation. The distributions of the maximum and minimum principal horizontal stress are shown in Fig. 3b, c. In particular, the minimum principal horizontal stress varied from 7.6 to 8.4 MPa, which is similar to the result of the back calculation. From 340 to 400 m, the minimum principal horizontal stress increased slightly due to disturbance caused by excavation activities. The distribution of the maximum principal horizontal stress is uniform (Fig. 3c). The maximum principal horizontal stress remained constant at 10.0 MPa, except locally at 480 and 250 m where it increased to 13 and 28.8 MPa, respectively.

2.2 Temporal–Spatial Characteristics of the Fracture Field

At present, the number of mechanical experiments being conducted to determine the temporal–spatial characteristics of the fracture fields of coal–rock masses in steeply inclined coal seams has decreased because that majority of fracture monitoring facilities could not be simulated by the loading equipment. For this reason, we developed a new experimental setup for rock mechanics that uses DR scanning. The schematics of the facility are shown in Fig. 4. The loading mode used was real-time loading and unloading conditions with a maximum load of 20 tons. The DR model used was DSM-80. 2D multimedia images of the internal fractures were constructed from the DR scanning results. The coal–rock mass sample preparation was carried out in strict accordance with the IRTM method recommended by ISRM and the samples were cube with side length equal to 60 mm.

In the mechanical experiment used to determine the temporal–spatial characteristics of the fracture fields of coal masses, the DR scanning settings used were 80 kVp, 320 mA, and 80 ms. There were three real-time loading and unloading stages: 0–3.48–1.77 MPa, 1.77–4.27–3.95 MPa and 3.97–9.68–0 MPa. Figure 5 shows all of the experimental results including the surface state, the DR scanning, and the post-processing images. We used MATLAB to apply the binarization process to the DR scanning results. In the process, the photic zone of the DR scanning images was defined as 1, and the opaque region was defined as 0. Relevant data from the DR scanning vectorization was used to determine the

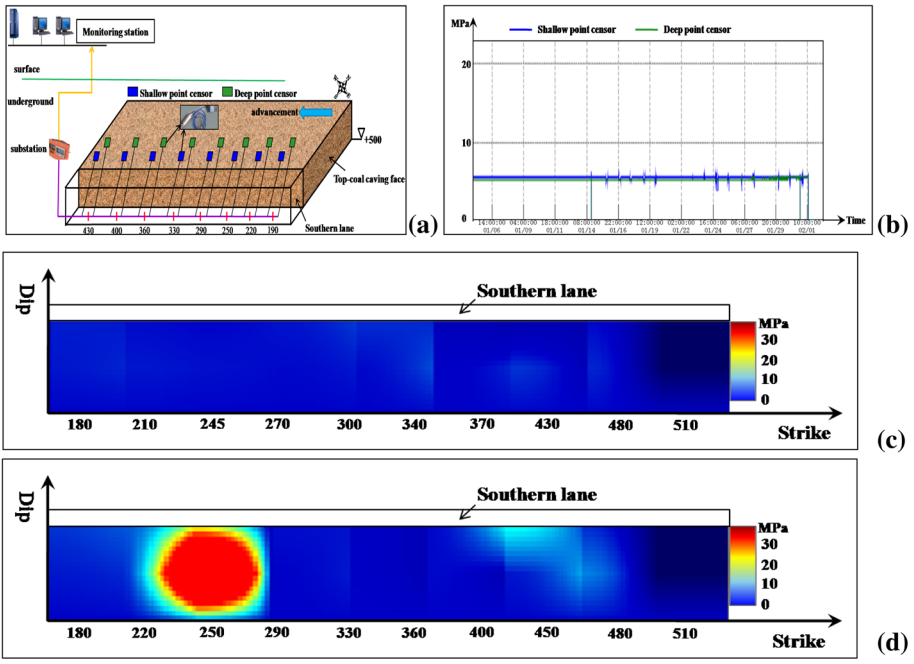

Fig. 3 Results of in situ monitoring of the regional geostress **a** Layout of geostress monitoring system; **b** vertical geostress; **c** minimum principal horizontal stress; and **d** maximum principal horizontal stress

quantitative parameters of the fracture field for use in the subsequent coupling numerical simulation.

Figure 5a shows the experimental results for the unload condition. When the peak value of the external loading (σ_p) increased to 3.48 MPa (Fig. 5b), fractures initiated and propagated in the direction of the external loading. A few of the fractures in the lower right corner of the coal sample began to propagate and turned into a main fracture. After unloading, the aperture of the main fracture increased significantly. When σ_p reached 4.27 MPa (Fig. 5c), the main fracture had progressed through the coal sample in the direction of the macroscopic fracture plane. Due to the continuous expansion of the fractures, faulting and displacement of the coal sample occurred in the lower right corner where the coal sample failed first after the next unloading stage. At the end of the experiment, σ_p was 9.68 MPa and conjugate fracture had developed (Fig. 5d). Stress concentration occurred in the residual pillar. In addition, X-ray attenuation occurred in the residual pillar due to further compaction of the coal pillar.

The same testing procedure was used for the rock sample. The DR scanning settings were 150 kVp, 320 mA, and 50 ms. Figure 5e shows the experimental results in the unload condition. There were no obvious initial fractures in the rock sample. σ_p was increased to 10.70 MPa in the first loading and unloading stage (Fig. 5f), and abundant small aperture fractures initiated extending from the edge of the rock sample to the center of the sample. When σ_p was increased to 14.65 MPa (Fig. 5g), the fractures propagated further and multiple fractures converged to form main fracture. Simultaneously, the slightly oblique fractures cut across the main fracture. At the end of the experiment, σ_p was 20.12 MPa (Fig. 5h), and the direction of the macroscopic fracturing plane was parallel to the radial

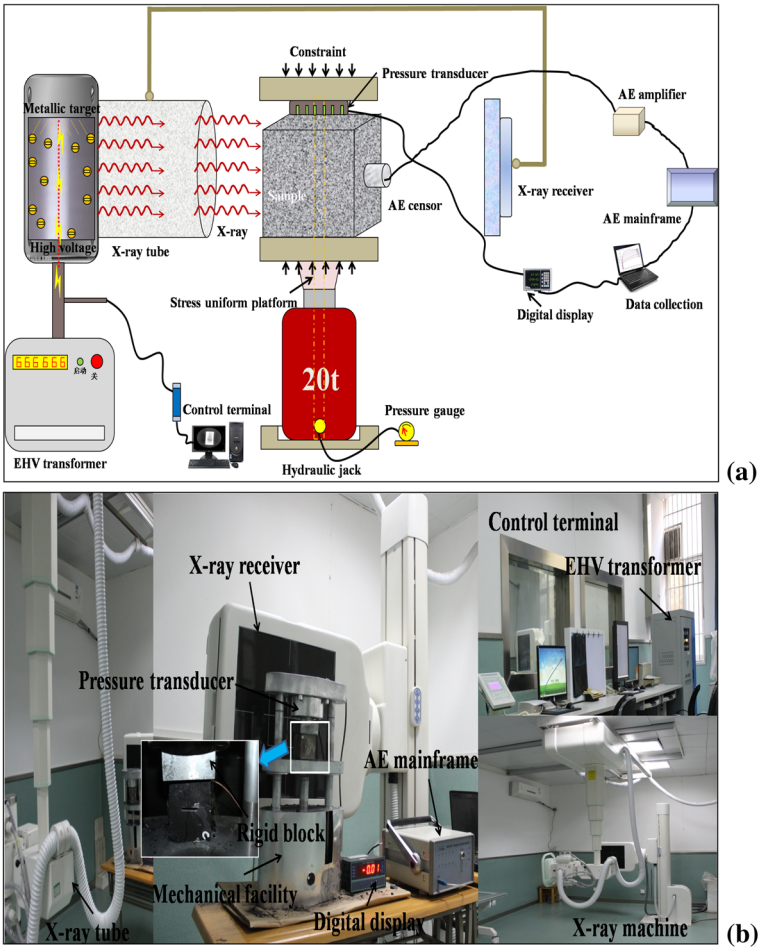

Fig. 4 Results on in situ monitoring of regional geostress **a** Layout of geostress monitoring system; **b** vertical geostress; **c** minimum horizontal principal stress; **d** maximum horizontal principal stress

direction. An X-shaped crack field was formed by the main fracture and the oblique fracture.

2.3 Development of the Coupled Computation Model

This paper presents a model of the fluid–solid coupling that occurs during the failure of a fractured coal–rock mass that takes into account the regional geostress characteristics obtained from the COMSOL Multiphysics software. The finite element method (FEM) was used as the theoretical basis for the COMSOL Multiphysics computations. Using a partial differential equation set solution, the coupling effect of the coal–rock mass combined with fluid and stress was scientifically determined. The coal–rock mass was regarded as a multiphase dielectric body. Hybrid seepage indexes including the porosity, permeability, hydraulic pressure, surface velocity, streamline, and outlet velocity were used to quantitatively analyze

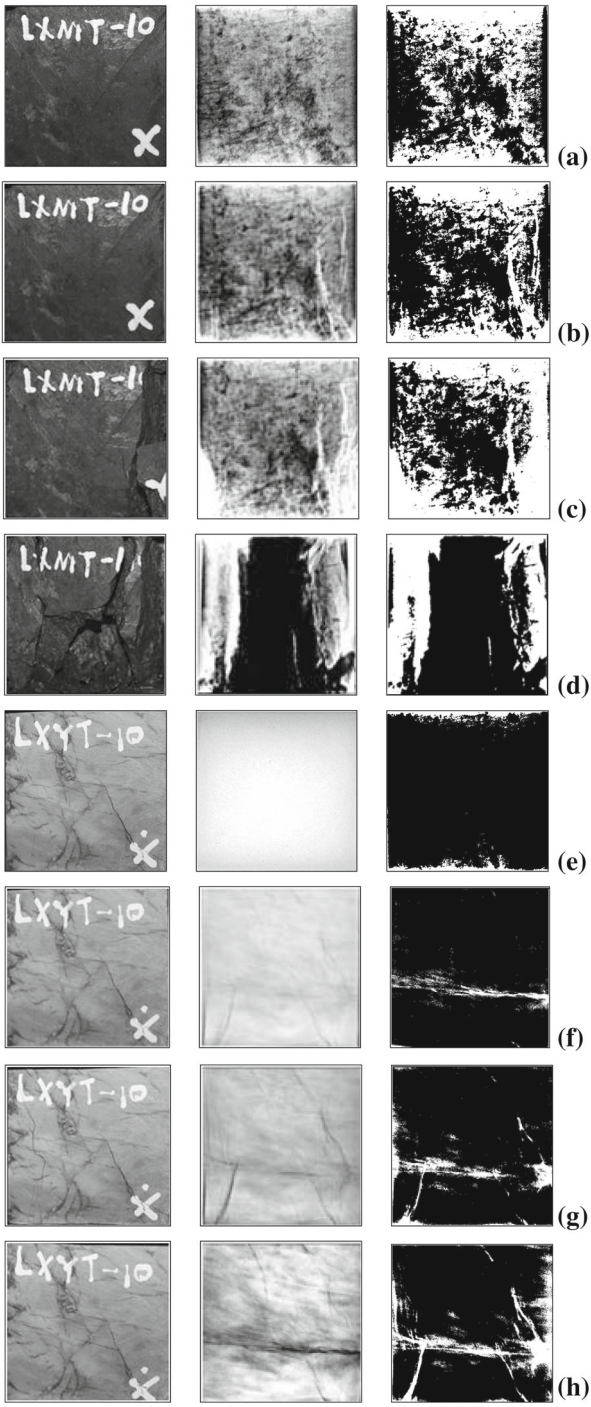

Fig. 5 Surface states of the coal–rock mass and relative results of both the DR scanning and the binarization process, size length of the coal–rock mass sample is 60 mm **a** external loading = 0 MPa (coal mass); **b** external loading = 3.48 MPa (coal mass); **c** external loading = 4.27 MPa (coal mass); **d** external loading = 9.68 MPa (coal mass); **e** external loading = 0 MPa (rock mass); **f** external loading = 10.70 MPa (rock mass); **g** external loading = 14.65 MPa (rock mass); and **h** external loading = 20.12 MPa (rock mass)

the fluid seepage through the coal–rock mass. When determining the regional geostress, the average and overall continuous properties were used to describe the continuous equation of water flow for a given set of conditions. Most previous studies adopted a modified form of Darcy's law to establish the overall average variables, e.g., the average velocity and overall throughput, for the governing equation. However, the accuracy of the computation results will be significantly increased by the improvements we have made in this study. Considering the structural differences that exist throughout the coal–rock mass, it was assumed that the fluid density and temperature within the fractures was constant and could not be compressed. The Navier–Stokes equation was introduced for the coupled computation as shown in Eq. (7).

$$-\nabla \boldsymbol{p} + \nabla \boldsymbol{\mu}(\nabla \boldsymbol{v} + \nabla \boldsymbol{v}^{\mathbf{T}}) = 0. \tag{7}$$

where p is the water injection pressure of the coal–rock mass; μ is the water viscosity coefficient; and v is the water flow velocity (m/s). In previous experiments, the water flow velocity was found to range from 9.6×10^{-3} to 9.0×10^{-2} m/s. Laminar flow occurred within the coal–rock mass due to a larger flow velocity. Slip occurred between the crack and the water, so the shear energy could not be ignored in the coupled computation. The Brinkman equation, as shown in Eq. (8), was suitable for the coupled computation for faster flow, which optimized Eq. (7) and fully took into account the viscosity and shear parameters that precisely describe the kinetic energy dissipation.

$$\begin{cases} \rho_{\mathrm{s}}[\partial(1-\varepsilon)/\partial t + \nabla v_{\mathrm{s}}(1-\varepsilon)] = 0 \\ \rho \mathbf{d} v_{\mathrm{s}}(1-\varepsilon)/\mathbf{d}t = -\mu(v - v_{\mathrm{s}})/k \end{cases}. \tag{8}$$

where ρ_{s} is the mass density of the coal–rock mass; ρ is the water density; and v_{s} is the displacement velocity. The coal–rock mass were fixed in our model, so v_{s} is 0, and k is the initial permeability of the coal–rock mass. Figure 6 shows a schematic of the coupled computation model. The model was 0.06×0.06 m. The entire rectangular region was regarded as the computation area. External loading was imposed on the top of the model at values of 3.48, 4.27, and 9.68 MPa. Similarly, the external loading of the rock mass was 10.70, 14.65, and 20.12 MPa in the above-mentioned mechanical experiment. The bottom of the model was fixed, and the lateral boundary of the model was symmetric with no confining pressure and limited displacement. Water was injected from the top of model. The water injection pressures (WIP) were 1.5, 3.5, 4.5, and 6.5 MPa, which are consistent with in situ water injection pressures in engineering projects. Accordingly, the values for the rock mass were 2.0, 5.0, 8.0, and 10.0 MPa. In addition, the water pressure at the outlet was equal to the water injection pressure. The body force caused by gravity was not considered in the simulation.

3 Simulation Results and Discussion

3.1 Permeability and Average Porosity

The following discussion involves the comprehensive analysis of the evolution mechanism of the porosity, permeability, hydraulic pressure, surface velocity, streamline, and outlet velocity. Our goal is to determine the temporal–spatial transformation of the seepage in the coal–rock mass, which have a large impact on the regional geostress and rock structure. Figure 7 illustrates the permeability and average porosity of the coal–rock mass during the

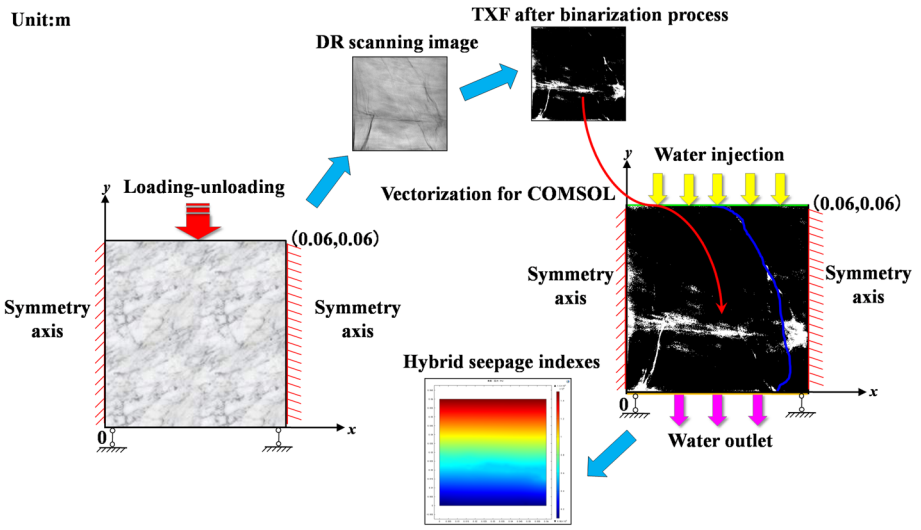

Fig. 6 Schematic of the coupled computation model for fluid–solid coupling during failure of a fractured coal–rock mass that takes into account the regional geostress characteristics based on the COMSOL Multiphysics software

entire coupled simulation. The calculations for permeability (k_{ave}) and average porosity (φ_{ave}) for a coupled condition are listed as Eqs. (9) and (10), respectively.

$$\begin{cases} \varphi_{ave-1} = \varphi_0 \times \mathrm{im}(x, y) \times S_1/S_0 + \mathrm{abs} \\ \varphi_{ave-2} = \varphi_{ave-1} \times \mathrm{im}(x, y) \times S_2/S_0 + \mathrm{abs} \\ \varphi_{ave-3} = \varphi_{ave-2} \times \mathrm{im}(x, y) \times S_3/S_0 + \mathrm{abs} \end{cases} \tag{9}$$

$$\begin{cases} k_{ave-1} = k_0 \times [100 \times (-\mathrm{im}(x, y) + 1) + \mathrm{abs}] \times S_1/S_0 \\ k_{ave-2} = k_{ave-1} \times [100 \times (-\mathrm{im}(x, y) + 1) + \mathrm{abs}] \times (\varphi_{ave-2}/\varphi_{ave-1})^3 \\ k_{ave-3} = k_{ave-2} \times [100 \times (-\mathrm{im}(x, y) + 1) + \mathrm{abs}] \times (\varphi_{ave-3}/\varphi_{ave-2})^3 \end{cases} \tag{10}$$

where φ_0 is the initial permeability and k_0 is the average porosity. im(x,y) is specific image function. S_0 is the initial value of image trait parameter. S_1, S_2 and S_3 are, respectively, values of the image trait parameter in different loading status. The initial permeability and average porosity of the coal mass and rock mass were 1.87×10^{-7} mm^2 and 7.35%, 4.85×10^{-6} mm^2 and 3.26%, respectively. The abs was 2.2×10^{-16}, which is regarded as the minimal value in the calculation. The calculation results are presented in Table 2. The results indicate that the variation of the permeability and average porosity are approximately the same for each external loading increment. The permeability and average porosity are positively correlated with the external loading level, and the peak permeability was 4.52×10^{-5} mm^2. As the external loading increased, the internal fractures propagated further and macro-fractures occurred in the model. This accounts for the continuous increase in the permeability and average porosity of the coal–rock mass.

3.2 Distribution of Water Pressure

Figure 8 shows the contour lines of the water pressure throughout the coal–rock mass for various external loadings. The contour lines are similar for identical external loading con-

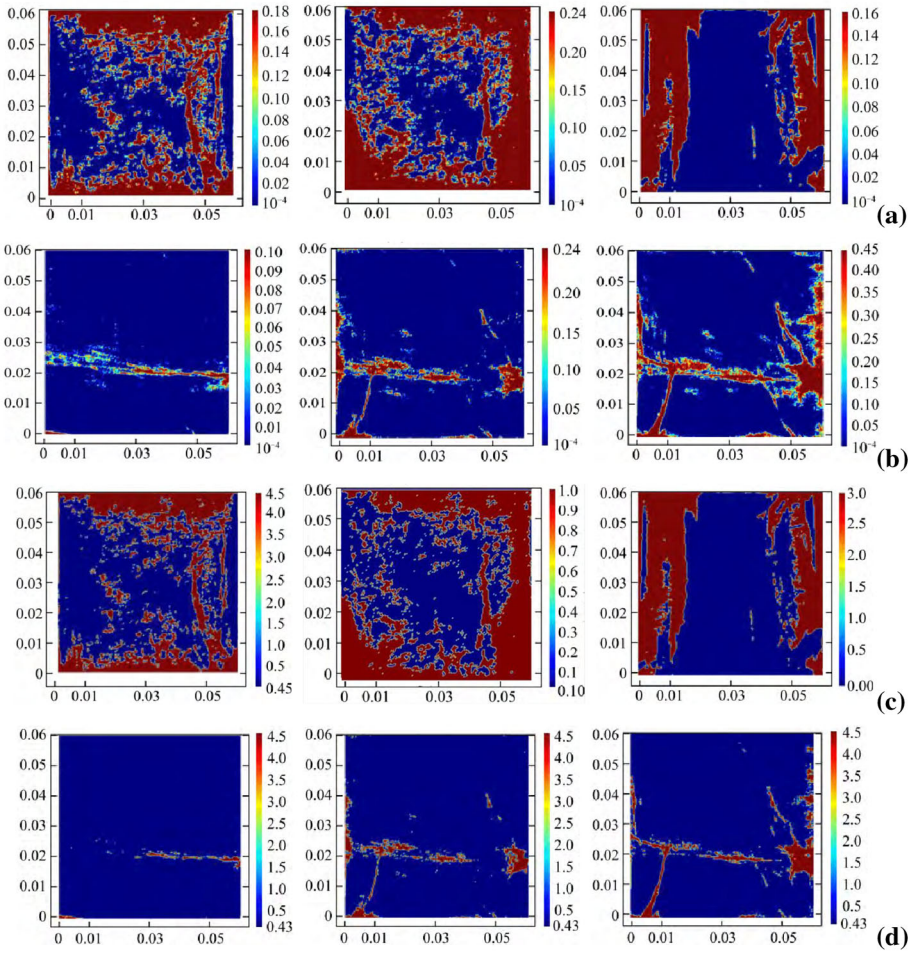

Fig. 7 Distribution of the average porosity and permeability of the coal–rock mass **a** average porosity of the coal mass; **b** average porosity of the rock mass; **c** permeability of the coal mass; and **d** permeability of the rock mass

ditions. However, the hydraulic gradient increased with increasing water injection pressure. The maximum water pressures within the coal mass and the rock mass were 6.3 and 9.9 MPa, respectively. The laminar flow within the rock mass was significant and obvious stress concentration occurred at the water injection point and the water outlet. In particular, the locations of stress concentration moved gradually closer to the water outlet as the external loading was increased. Before water flowed through the main fracture in the center of the rock mass, the water was evenly distributed and the hydraulic gradient consistently decreased. When water flowed were through the main fracture, the hydraulic gradient abruptly decreased. Similarly, the hydraulic gradient decreased closer to the water injection area, and the hydraulic gradient increased significantly as the y coordinate value increased.

Table 2 Calculated average porosity and permeability of the coal and rock masses

Rock type	External loading (MPa)	Average porosity (%)	Permeability (mm^2)
Coal mass	3.48	11.74	4.54e–06
	4.27	18.89	1.04e–06
	9.68	27.65	3.33e–05
Rock mass	10.70	4.11	4.78e–07
	14.65	8.25	5.90e–06
	20.12	21.25	4.52e–05

3.3 Distribution of Water Flow Velocity

Accurately describing the migration of the maximum water flow velocity is important when determining the temporal–spatial evolution characteristics of the fracture field in the coal–rock mass. Figure 9 shows a contour plot of the superficial distribution of the water flow velocity for various external loadings. The value of the water flow velocity is positively correlated with both the water injection pressure and external loading. The maximum water flow velocity within the coal mass occurred near the secondary fractures on the right side of the model or at the lower left and lower right corners of the water outlet, whereas the maximum water flow velocity within the rock mass occurred near the main fracture in the center of the model. Before σ_p reaches 9.68 MPa, the area of maximum water flow velocity was located on the right side of the coal mass, and the majority of the water flow discharged on the right side due to the fully developed fracture network. After the last loading stage, the area of maximum water flow velocity migrated to the left side of the coal mass, and the left side began to accommodate more of the outflow. Conversely, after the first loading stage, the area of maximum water flow velocity within the rock mass occurred near the center of the main fracture. The water flow velocity in other areas was negligible. This indicates that there was no overall fracture network within the rock mass. Furthermore, the average flow velocity increased significantly with increased external loading. At the end of the experiment, the area of maximum water flow velocity was located at the lower left corner of the water outlet.

3.4 Distribution of Seepage Streamline

Figure 10 illustrates the distribution of the seepage streamline and the water flow orientation. In Fig. 10, the black solid line is the water seepage streamline, and the red and blue arrows are the water flow orientation. The red arrows represent the principal orientation of the flow. The orientation of the water flow was consistent. In the streamline aspect, the distribution of the seepage streamline within the coal mass was very irregular and the water flow was too random. The distribution of the seepage streamline within the rock mass was exactly the opposite. It was approximately uniformly distributed along the x axis. However, the distribution of the seepage streamline became more random in specific areas below the main fracture with increased external loading. In addition, the main orientation of the water flow corresponded to the region of maximum flow velocity. There were a large number of water flow clusters near the rock-mass's fractures, which caused the amount of water outflow from the main fracture to decrease significantly. With increased external loading, new fractures emerged on both sides of the base, and the main water flow orientation migrated to the region.

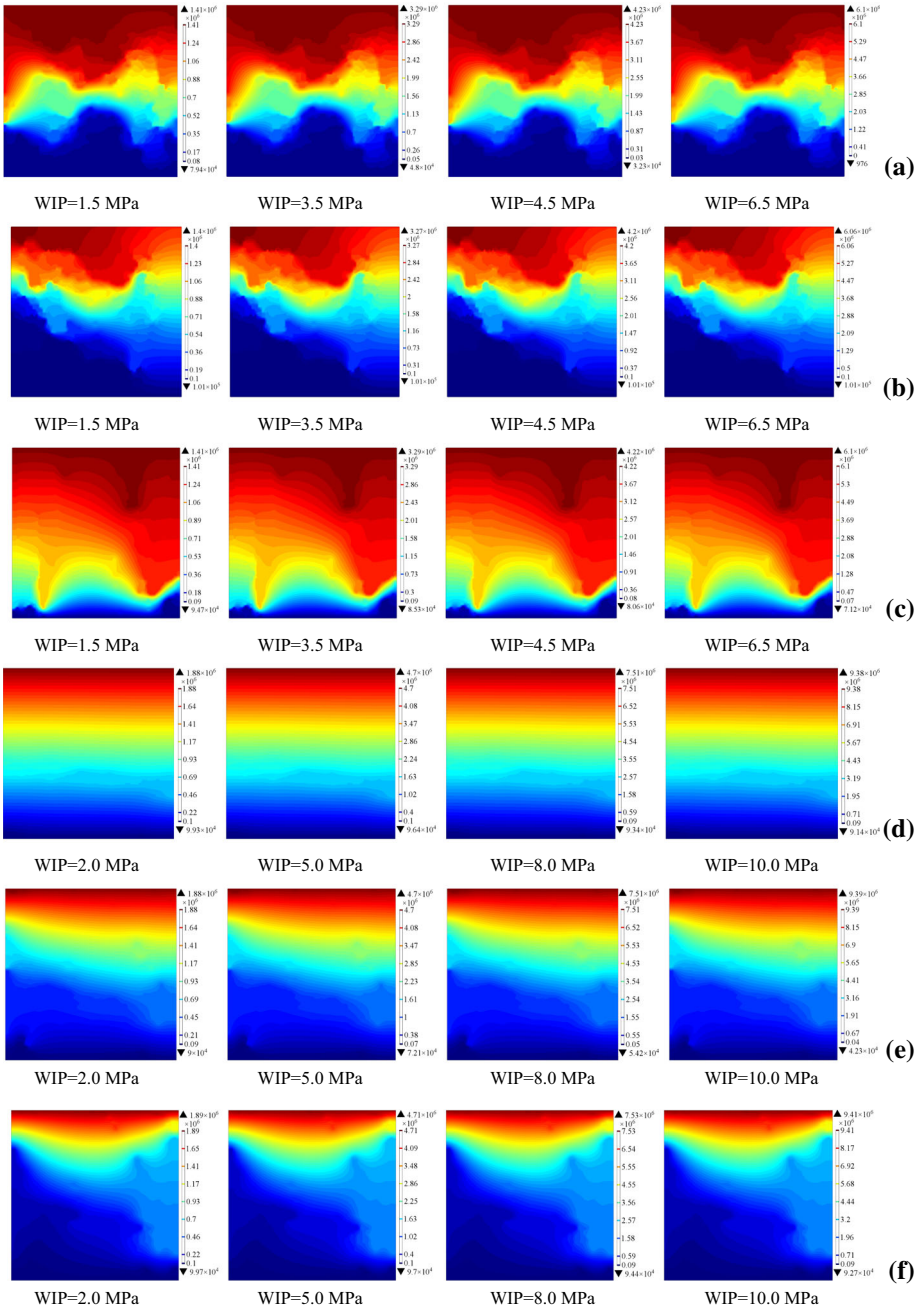

Fig. 8 Contour lines for the water pressure within the coal–rock mass for various external loading values **a** external loading = 3.48 MPa (coal mass); **b** external loading = 4.27 MPa (coal mass); **c** external loading = 9.68 MPa (coal mass); **d** external loading = 10.70 MPa (rock mass); **e** external loading = 14.65 MPa (rock mass); and **f** external loading = 20.12 MPa (rock mass)

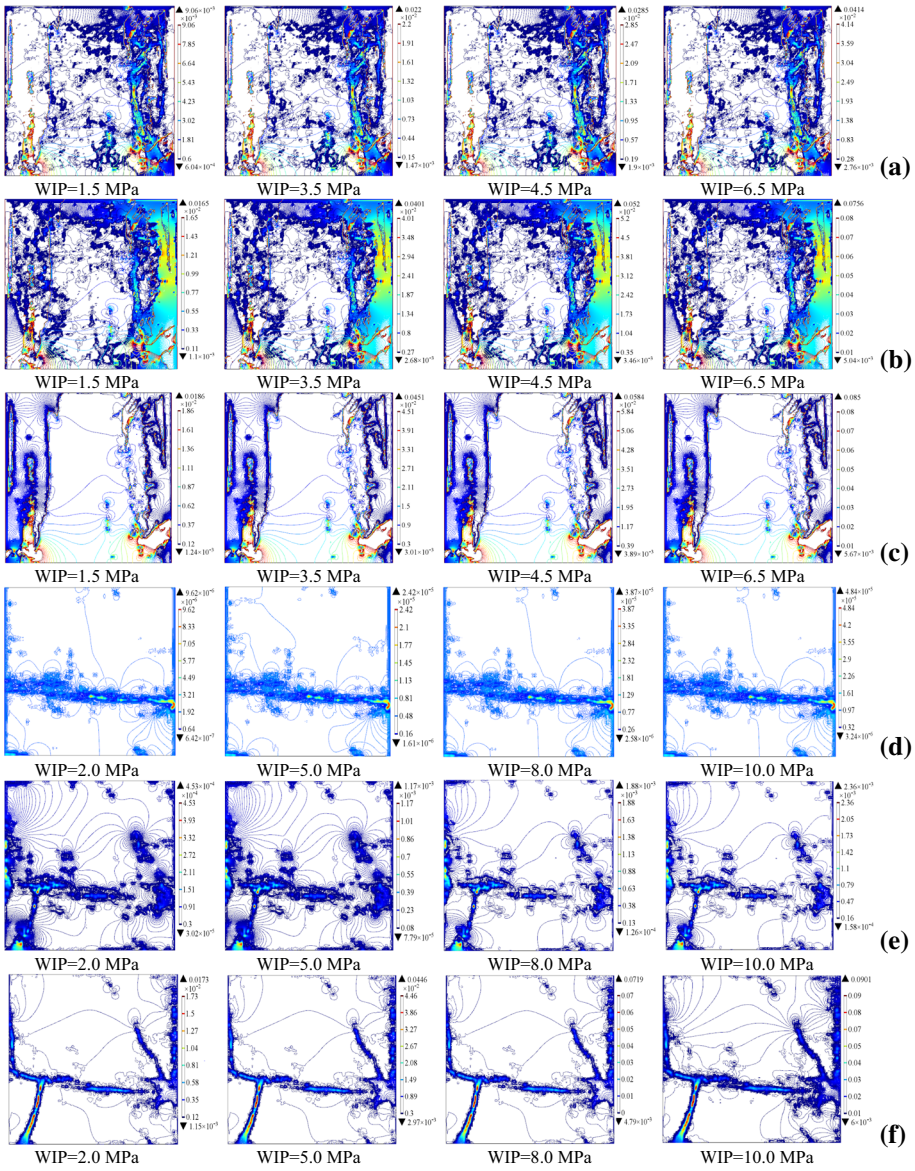

Fig. 9 Contour plots of the superficial distribution of the water flow velocity for various external loading values **a** external loading = 3.48 MPa (coal mass); **b** external loading = 4.27 MPa (coal mass); **c** external loading = 9.68 MPa (coal mass); **d** external loading = 10.70 MPa (rock mass); **e** external loading = 14.65 MPa (rock mass); and **f** external loading = 20.12 MPa (rock mass)

3.5 Flow Velocity in the Water Outlet

Figure 11 shows plots of the *y*-direction component of the water flow velocity at the water outlet for different × coordinates. During the model design, ten real-time water flow velocity monitoring points were set up uniformly along the water outlet. The velocity component was negative because the flow orientation was opposite to the upward (positive) direction of the

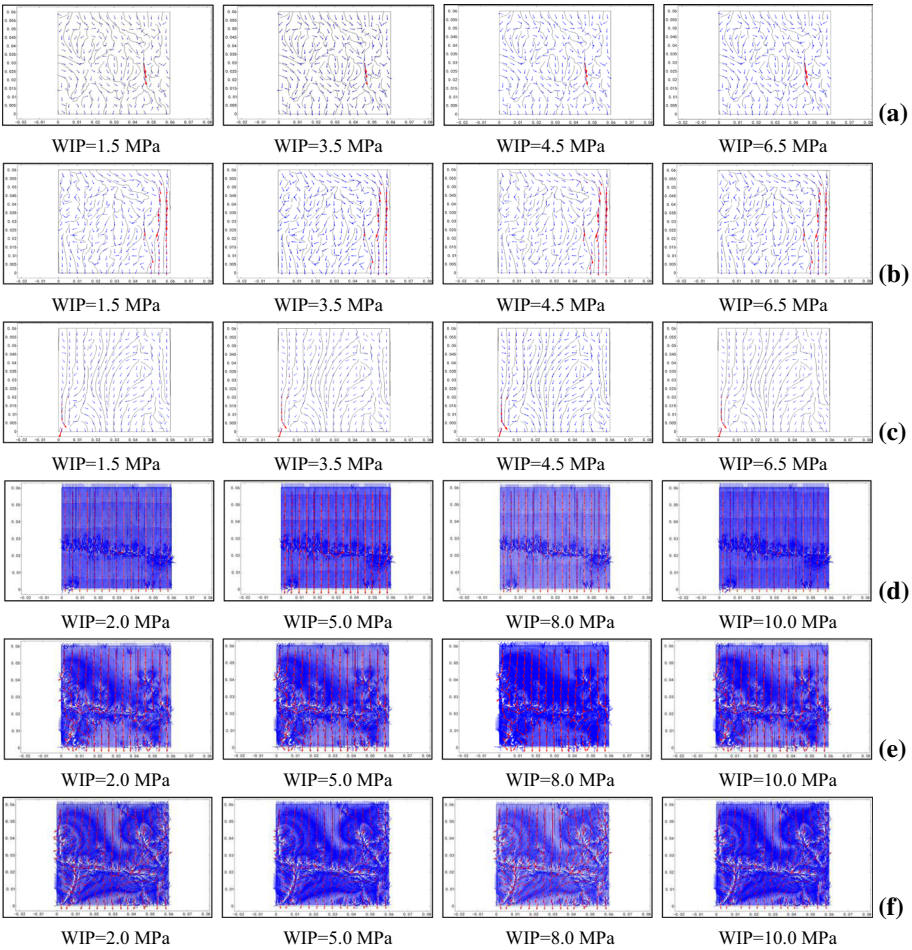

Fig. 10 Distribution characteristics of the streamline and water flow orientations for various external loading values **a** external loading = 3.48 MPa (coal mass); **b** external loading = 4.27 MPa (coal mass); **c** external loading = 9.68 MPa (coal mass); **d** external loading = 10.70 MPa (rock mass); **e** external loading = 14.65 MPa (rock mass); and **f** external loading = 20.12 MPa (rock mass)

y axis. As can be seen from Fig. 11, the maximum of the water flow velocity component is located at both sides of the model and increases with increasing external loading. The maximums for the coal mass and rock mass were 0.038 and 0.022 m/s, respectively. The variation in the velocity component is consistent with the different WIP values. The water flow velocity increased with increasing WIP. In the rock mass, some extreme points emerged on all of the velocity component curves.

4 Conclusions

We used the back calculation method to predict the regional geostress. According to in situ stress monitoring, the accuracy of the back calculation is verified, and the vertical stress

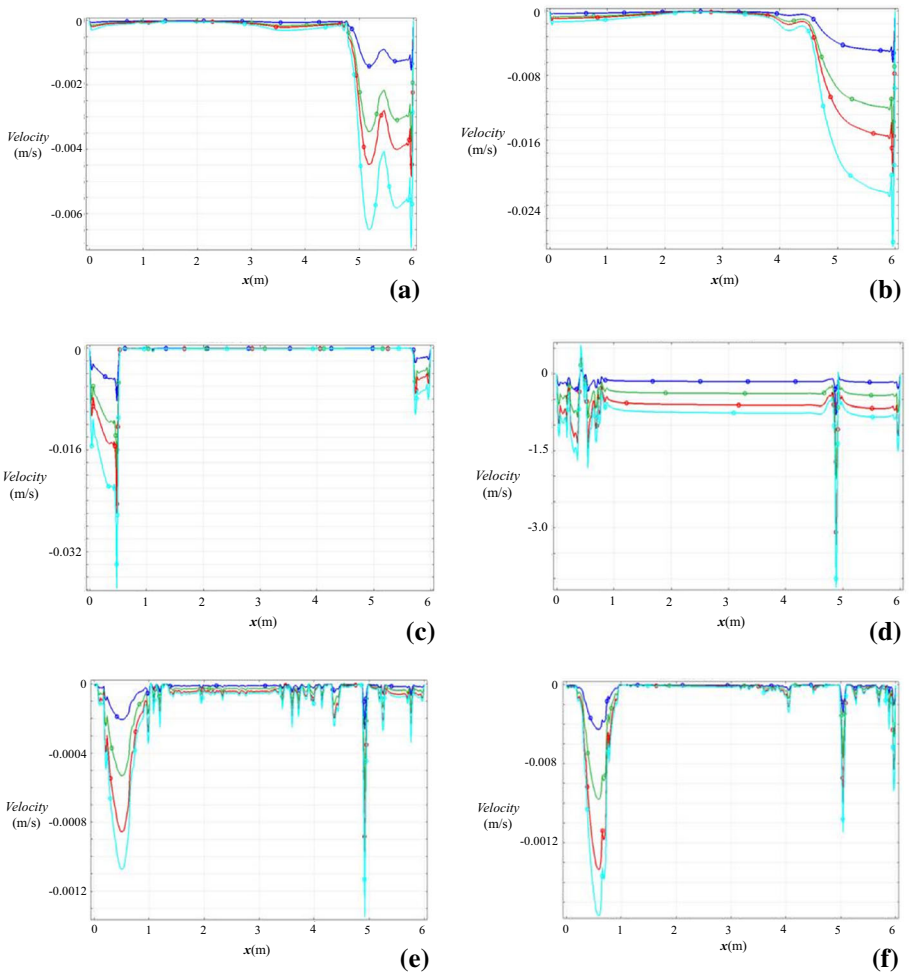

Fig. 11 Distribution characteristics of the *y*-direction component of the water flow velocity versus × coordinate position **a** external loading = 3.48 MPa (coal mass); **b** external loading = 4.27 MPa (coal mass); **c** external loading = 9.68 MPa (coal mass); **d** external loading = 10.70 MPa (rock mass); **e** external loading = 14.65 MPa (rock mass); and **f** external loading = 20.12 MPa (rock mass)

and minimum principal horizontal stress used in the numerical simulation are 7.057 and 8.085 MPa, respectively. In addition to being comparable to the stable vertical stress and the minimum principal horizontal stress, the maximum principal horizontal stress contains a local undulation due to disturbances from nearby excavation.

A newly developed mechanical experimental system for DR scanning was presented and was used to determine the temporal–spatial evolution characteristics of the fracture field, which were used along with the DR scanning data that were processed using binarization in the mechanical experiment. Simultaneously, the temporal–spatial evolution characteristics of the fracture field in both the coal mass and the rock mass were determined from the experiment. The main fractures continued to propagate with increasing external loading, and the spatial form of the fracture fields is X-shaped.

This paper presents a model for fluid–solid coupling during the failure of a fractured coal–rock mass that takes into account the regional geostress characteristics based on the COMSOL Multiphysics software. The results indicate that the primary factor causing fracture propagation and connection is increased external loading, which leads to the development of macro-fractures in the coal–rock mass and increased average porosity and permeability. The flow within the maximum velocity region represents the distribution characteristics of the induced cracks. The peak flow velocity occurs at the main fracture and in the direction of the water injection pressure (WIP). Smaller fractures have a larger hydraulic gradient and a larger flow velocity. The characteristics of the velocity at the water outlet indicate that the maximum flow velocity at the outlet occurs at two sides of the model and increases with increasing external loading. The fluid–solid coupling mechanisms would provide a reliable theoretical basis for optimization of mined-void roof weakening in mining the steeply inclined coal seam.

Acknowledgements Financial support for this work was provided by the 973 Key National Basic Research Program of China (No. 2015CB251602), the National Natural Science Foundation of China (No. 51504184, No. 51604264), the China Postdoctoral Science Foundation (No. 2017M196372XB), the Doctoral and Post-doctoral Start Foundation of Xi'an University of Science and Technology (No. 2016QDJ048, No. 2017QDJ060), and the Open Projects of Research Center of Coal Resources Safe Mining and Clean Utilization, Liaoning (No. LNTU17KF08). Support from these agencies is gratefully acknowledged.

References

Alehossein, H., Poulsen, B.A.: Stress analysis of longwall top coal caving. Int. J. Rock Mech. Min. Sci. **47**(1), 30–41 (2010)

Feng, X.T., Masahiro, S.: Rock fracturing behaviors under chemical corrosion—Part I: experimental study. Chin. J. Rock Mech. Eng. **19**(4), 403–407 (2000). **(in Chinese)**

Hatheway Allen, W., Kanaori, Y.J., et al.: Encompassing hydrogeology, environmental geology and the applied geosciences. Eng. Geol. **81**(2), 99–130 (2005)

Huang, R.Q., Xu, D.M., Fu, X.M., et al.: Development and research of high pressure permeability testing system for rocks. Chin. J. Rock Mech. Eng. **27**(10), 1981–1991 (2008). **(in Chinese)**

Jafari, M.K., Pellet, F., Boulon, M.: Experimental study of mechanical behavior of rock joints under cyclic loading. Rock Mech. Rock Eng. **37**(1), 3–7 (2004)

Kelly, M., Balusu, R., Hainsworth, D.: Status of longwall research in CSIRO. In: Proceedings of 20th International Conference on Ground Control in Mining, Morgantown, vol. 16 (2001)

Lai, X.P., Shan, P.F., Cao, J.T., et al.: Hybrid assessment of pre-blasting weakening to horizontal section top coal caving (HSTCC) in steep and thick seams. Int. J. Min. Sci. Technol. **24**(1), 31–37 (2014)

Lai, X.P., Shan, P.F., Cao, J.T., et al.: Simulation of asymmetric destabilization of mine-void rock masses using a large 3D physical model. Rock Mech. Rock Eng. **49**(2), 487–502 (2016)

Lauriello, P.J., Fritsch, C.A.: Design and economic constraints of thermal rock weakening techniques. Int. J. Rock Mech. Min. Sci. GeoMech. **11**(1), 31 (1974)

Oda, M.: An equivalent continuum model for coupled stress and fluid flow analysis in jointed rock masses. Water Resour. Reserv. **22**(13), 1845–1856 (1986)

Scesi, L., Gattinoni, P.: Roughness control on hydraulic conductivity in fractured rocks. Hydrogeol. J. **15**(2), 201–211 (2007)

Simsir, F., Ozfirat, M.K.: Determination of the most effective longwall equipment combination in longwall top coal caving (LTCC) method by simulation modeling. Int. J. Rock Mech. Min. Sci. **45**(6), 1015–1023 (2008)

Tang, L.S., Zhang, P.C., Wang, S.J.: Testing study on effects of chemical action of aqueous solution on crack propagation in rock. Chin. J. Rock Mech. Eng. **21**(6), 822–827 (2002). **(in Chinese)**

Tang, H.M., Jia, H.B., Hu, X.L., et al.: Characteristics of landslides induced by the great wenchuan earthquake. J. Earth Sci. **21**(1), 104–113 (2010)

Wang, Y., Su, B.Y., Xu, Z.Y.: Comment on the models of seepage flow in fractured rock masses. Adv. Water Sci. **7**(3), 276–282 (1996)

Wu, Y.Q.: Study of Seepage law with stress in jointed rock masses. Hydrogeol. Eng. Geol. **22**(6), 30–35 (1995). **(in Chinese)**

Xie, Y.S., Zhao, Y.S.: Numerical simulation of the top coal caving process using the discrete element method. Int. J. Rock Mech. Min. Sci. **46**(6), 983–991 (2009)

Xie, H.P., Gao, F., Ju, Y.: Research and development of rock mechanics in deep ground engineering. Chin. J. Rock Mech. Eng. **34**(11), 2161–2178 (2015). **(in Chinese)**

Zhang, Z.F., Lai, X.P.: Segment pre-blasting of sublevel caving of steep and thick coal seam under complex conditions. J. Chin. Coal. Soc. **33**(8), 845–847 (2008). **(in Chinese)**

Zhang, Y.Z., Zhang, J.C.: Experimental study of the seepage flow-stress coupling in fractured rock masses. Rock Soil. Mech. **18**(4), 59–62 (1997). **(in Chinese)**

Zhang, D.S., Li, W.P., Lai, X.P., et al.: Development on basic theory of water protection during coal mining in northwest of China. J. Chin. Coal. Soc. **42**(1), 36–42 (2017). **(in Chinese)**

Zhao, M., Zhou, H., Chen, D.: Investigation and application on gas drive development in ultra-low permeability reservoirs. J. Hydrogeol. **20**(2), 254–260 (2008)

Zhu, W.C., Wei, C.H., Tian, J., et al.: Coupled thermal–hydraulic–mechanical model during rock damage and its preliminary application. Rock Soil. Mech. **29**(12), 2851–2857 (2009). **(in Chinese)**